https://doi.org/10.30799/jnst.361.25100302 J. Nanosci. Tech. - Volume 10 Issue 3 (2025) 1012–1018

Share Your Innovations through JACS Directory

Journal of Nanoscience and Technology

Visit Journal at https://www.jacsdirectory.com/jnst

ISSN: 2455-0191

Band Structure Engineering of $BaSrTiO_3$-ZnO Composites for Improved Water Splitting Performance

Seema Jangir, Manisha Singhal, Deepak Singh Rajawat*

Department of Chemistry, IIS(Deemed to be) University, Jaipur – 302 020, Rajasthan, India.

ARTICLEDETAILS

Article history:
Received 06 October 2025
Accepted 22 October 2025
Available online 31 October 2025

Keywords:
Photocatalysis
Hydrogen Production
$BaSrTiO_3$-ZnO Composites
Heterojunction
Water Splitting

ABSTRACT

Barium strontium titanate ($BaSrTiO_3$) and zinc oxide (ZnO) composites as photocatalysts for hydrogen production through water splitting is the promising composite material because of the synergistic effects of its components. $BaSrTiO_3$ has a strong built-in electric field that helps separate charge carriers, while ZnO offers high electron mobility. The formation of a heterojunction at their interface improves charge transfer and reduces electron-hole recombination, which are major limitations in other systems. The BST@ZnO composites demonstrated markedly enhanced photocatalytic performance, with 3% and 5% samples showing the highest photocurrent density (~2.8 $mAcm^{-2}$) due to efficient charge separation and low charge-transfer resistance. Electrochemical analyses confirmed improved carrier mobility and interfacial conductivity, validating the role of engineered heterojunctions in accelerating HER kinetics. Although OER activity remained limited, the composites exhibit excellent potential for hydrogen-focused photocatalytic applications, bridging material design with sustainable energy generation.

1. Introduction

The transition toward clean and renewable energy systems is imperative in the face of rising global energy consumption and environmental degradation caused by fossil fuel dependence. Hydrogen, with its high energy content and zero-emission profile, is a leading candidate for sustainable energy carriers [1]. Traditional hydrogen production methods such as steam methane reforming not only rely on finite fossil resources but also generate significant carbon emissions, undermining their environmental viability. Photocatalytic water splitting presents a greener alternative by leveraging solar energy to dissociate water molecules into hydrogen and oxygen, thereby providing a sustainable route for hydrogen generation [2]. However, major bottlenecks such as inadequate visible light absorption, rapid recombination of photoinduced charge carriers, and photocatalyst instability restrict the widespread deployment of this technology. Hydrogen, with its high energy density and zero-carbon emissions, has emerged as a promising alternative to fossil fuels and a clean energy carrier [3]. However, traditional hydrogen production methods such as steam methane reforming remain heavily reliant on fossil fuels and contribute substantially to greenhouse gas emissions, thereby necessitating the search for cleaner alternatives. Photocatalytic water splitting has garnered significant attention as a sustainable hydrogen production method, as it mimics natural photosynthesis to convert solar energy into chemical energy using semiconductor photocatalysts [4]. Despite its promise, the practical application of this method is hindered by several limitations, including low visible light absorption, rapid charge carrier recombination, and photocorrosion of photocatalysts [5].

To address these issues, composite materials integrating multiple semiconductors have been explored for their ability to enhance photocatalytic efficiency [6]. Among these, barium strontium titanate ($BaSrTiO_3$ or BST) and zinc oxide (ZnO) composites have shown great promise due to their complementary electronic and structural properties [7]. $BaSrTiO_3$, a perovskite-structured ferroelectric material, features a high dielectric constant and a strong internal electric field, promoting efficient charge separation and transport [7]. However, its relatively wide bandgap limits its absorption of visible light. ZnO, a direct-bandgap semiconductor with excellent UV light absorption and high electron mobility, faces challenges with fast electron-hole recombination and photocorrosion [8]. The combination of BST and ZnO in a heterojunction structure addresses these limitations, improving charge transfer, reducing recombination losses, and extending light absorption into the visible spectrum [9]. Recent studies underscore the enhanced photocatalytic performance of BST-ZnO composites in solar-driven hydrogen generation. These include the implementation of core-shell nanostructures like $BaTiO_3$@$SrTiO_3$ in sono photocatalytic systems, as well as hybrid composites such as ZnO/$SrTiO_3$ and ZnO-$BaTiO_3$ that exhibit improved light absorption, electron mobility, and bandgap tenability [10-13]. The interface-driven charge separation enabled by the built-in electric field at the BST-ZnO junction plays a critical role in facilitating the hydrogen evolution reaction (HER), as does the increased surface activity achieved through doping and nano structuring. Nonetheless, issues related to limited visible light absorption and photocatalyst stability persist [14].

To overcome these remaining challenges, ongoing research focuses on bandgap engineering, plasmonic enhancement, and protective coatings to improve durability under illumination. Additionally, advanced synthesis techniques are being developed to control morphology and interface quality [15]. Integration into scalable devices such as photoelectrochemical cells and coupling with hybrid energy systems could further elevate the commercial viability of these materials. The application of machine learning for predictive material design offers a promising direction to accelerate discovery [16]. Future research should focus on the development of advanced synthesis methods to precisely control the morphology, composition, and band structure of $BaSrTiO_3$-ZnO composites. The integration of these materials into practical photocatalytic devices, such as photoelectrochemical cells and hydrogen generation systems, will be essential for scaling up hydrogen production for commercial applications [17]. Additionally, exploring hybrid approaches that combine photocatalysis with other renewable energy technologies, such as photovoltaic-electrochemical hybrid systems, could open new possibilities for improving efficiency and feasibility [18]. The application of machine learning and computational modelling in material design and optimization can further accelerate the discovery of high-performance $BaSrTiO_3$-ZnO composites with tailored properties for water splitting applications [19].

In this context, the present study aims to provide an in-depth investigation of $BaSrTiO_3$-ZnO composites, encompassing their synthesis, structural and optical characterization, and photocatalytic behaviour [20]. By examining the fundamental structure–property relationships, this work seeks to advance the development of efficient, robust, and scalable

*Corresponding Author:drdeepaksr@gmail.com(Deepak Singh Rajawat)

https://doi.org/10.30799/jnst.361.25100302

Cite this Article as: Seema Jangir, Manisha Singhal, Deepak Singh Rajawat, Band structure engineering of $BaSrTiO_3$-ZnO composites for improved water splitting performance, J. Nanosci. Tech. 10(3) (2025) 1012–1018.

photocatalytic systems for sustainable hydrogen production. In conclusion, $BaSrTiO_3$-ZnO composites represent a promising class of materials for solar-driven hydrogen production, combining the advantages of perovskite ferroelectrics and wide-bandgap semiconductors [21]. Their ability to facilitate efficient charge separation, enhanced light absorption, and tunable bandgap properties makes them highly suitable for photocatalytic applications. However, further research and technological advancements are needed to address current limitations and enable large-scale implementation [22]. By leveraging material innovations, advanced fabrication techniques, and interdisciplinary approaches, researchers can unlock the full potential of $BaSrTiO_3$-ZnO composites for driving the future of sustainable hydrogen energy production [23].

This work introduces a novel $BaSrTiO_3$–ZnO (BST–ZnO) composite system for photocatalytic water splitting, combining the ferroelectric properties of BST with the semiconducting behavior of ZnO to enhance charge separation and solar light absorption. Unlike previous studies that primarily focus on binary ZnO/$SrTiO_3$ or $BaTiO_3$ systems, this research uniquely employs a co-precipitation strategy with ultrasonication to ensure homogeneous dispersion and strong interfacial coupling.

2. Experimental Methods

2.1 Chemicals

The following chemicals were used in the synthesis of $BaSrTiO_3$-ZnO composites: Barium acetate ($Ba(CH_3COO)_2$) - American Elements; Strontium acetate ($Sr(CH_3COO)_2$)- Alfa Aesar; Titanium isopropoxide ($Ti[OCH(CH_3)_2]_4$)- Sigma-Aldrich (Merck); Acetic acid (CH_3COOH) - Merck KGaA; Ethanol (C_2H_5OH) - VWR (Avantor); Deionized water (H_2O)- Thermo Fisher Scientific; Zinc acetate ($Zn(CH_3COO)_2$) - Fisher Scientific and Sodium hydroxide (NaOH) – Millipore Sigma.

2.2 Synthesis of $BaSrTiO_3$ Nanopowder

The $BaSrTiO_3$ nanopowder was synthesized using sol-gel route as shown in Fig. 1. Barium acetate (0.04 mol) and strontium acetate (0.026 mol) were separately dissolved in 8 mL and 4 mL of acetic acid, respectively, and then mixed under continuous stirring. The pH of the solution was adjusted to remain between 3.5 and 5.0. Titanium isopropoxide (0.066 mol) diluted in 2 mL of ethanol was added dropwise to the solution, which was then refluxed at 125 °C for 2 hr. Upon cooling to 5 °C, deionized water was added to induce gelation. The resulting gel was dried at 200 °C for 2 hr and then calcined at temperature 850 °C for 2 hr to obtain nanocrystalline BST powder.

2.3 Synthesis of ZnO Nanostructures

Two-dimensional ZnO nanostructures were prepared via a co-precipitation method (Fig. 2) at room temperature. Equal volumes (10 mL) of 1 M zinc acetate and 8 M sodium hydroxide solutions were mixed with constant stirring for 30 min. The resulting white precipitate was diluted to 200 mL with deionized water, filtered, and thoroughly washed to remove residual ions and impurities. It was then dried to yield ZnO nanopowder.

2.4 Synthesis of $BaSrTiO_3$-ZnO Composites

To develop functionally enhanced BST@ZnO nanocomposites, a facile co-precipitation method was employed, integrating pre-synthesized BST nanopowder directly into the ZnO formation process as shown in Fig. 3. Zinc acetate solution (1 M) (10 mL) was first prepared and blended with varying concentrations of BST nanopowder (1-5 wt%) based on the total anticipated ZnO mass. The BST was homogeneously dispersed into the zinc precursor solution using ultrasonication for 30 minutes to ensure uniform mixing and prevent agglomeration. In parallel, 10 mL of 8 M sodium hydroxide solution was prepared and subsequently added dropwise to the BST–zinc acetate mixture under continuous stirring. This triggered the formation of a fine white precipitate, corresponding to BST-decorated ZnO nanostructures. The reaction was allowed to proceed for 30 minutes at room temperature to promote complete co-precipitation. The resulting suspension was then diluted to a total volume of 200 mL with deionized water to aid in purification. The precipitate was thoroughly filtered and washed multiple times to eliminate residual ions and impurities. Finally, the product was dried at 80-100 °C overnight to yield BST@ZnO nanocomposite powders with BST loadings of 1 - 5 wt% and named as BST@ZnO (1% - 5%). This in-situ incorporation of BST during ZnO synthesis not only ensures intimate interfacial contact but also effectively modulates the structural, electrical, and optical properties of ZnO-making the composites highly suitable for applications in sensors, tunable dielectrics, and multifunctional nano-devices.

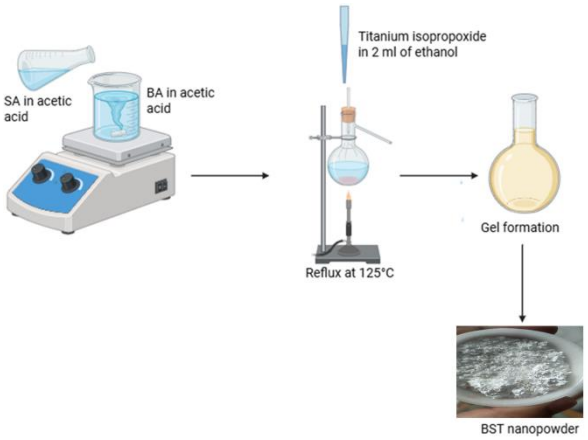

Fig. 1 Synthesis of BST nanopowder (SA - Stroncium Acetate & BA - Barium Acetate)

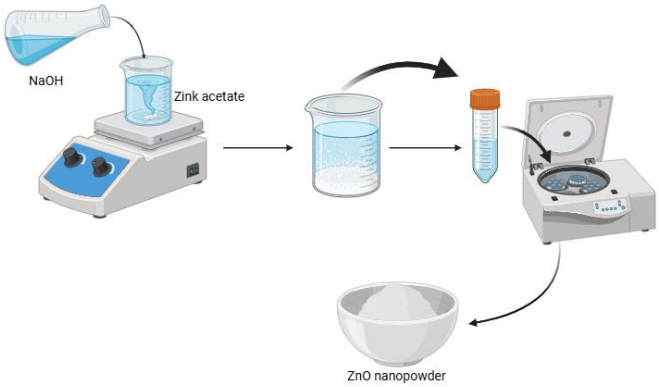

Fig. 2 Synthesis of ZnO nanopowder

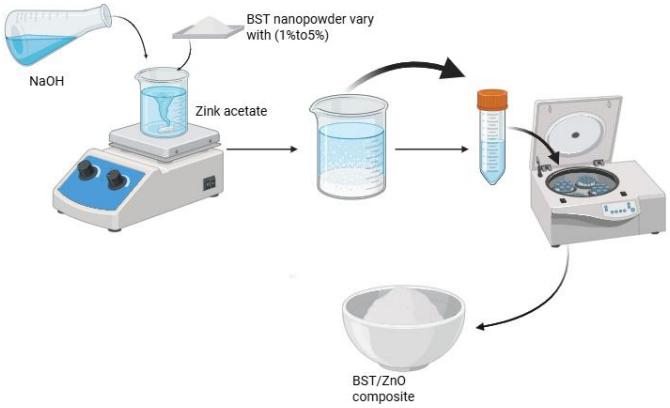

Fig. 3 Synthesis of BST/ ZnO composite

2.5 Material Characterization

The crystal structure and phase identification of the synthesized pure BST and ZnO and composites material were analysed using powder X-ray diffraction (XRD) with a Bruker D-8 diffractometer, scanning at 0.3° per second over a 2θ range of 10-80°. This technique helped to confirm the crystallinity and phase purity of the material. To identify functional groups and molecular interactions, Fourier transform infrared spectroscopy (FTIR) was performed using a Bruker Hyperion spectrometer within the 500-4000 cm^{-1} range. The optical properties of the material were studied through UV-visible absorbance spectroscopy using a Shimadzu spectrophotometer in the 300-800 nm range, which provided insights into its light absorption characteristics. The surface morphology and elemental composition of the samples were examined using field emission scanning electron microscopy (FE-SEM) and energy dispersive X-ray spectroscopy (EDX) with a TESCAN Magna microscope. These techniques allowed for a detailed analysis of particle size, shape, and elemental distribution.

The PEC performance of both pure BST and ZnO and composites samples was evaluated using a three-electrode system connected to a Zahner Zennium Pro electrochemical workstation. Indium tin oxide (ITO) glass plates coated with served as the working electrodes, with a platinum wire as the counter electrode and an Ag/AgCl electrode as the reference. The electrolyte used was a 0.5 M Na_2SO_4 aqueous solution with a neutral pH 6. To fabricate the working electrode, 100 mg BST/Zno composites was mixed with 100 µL of Nafion solution and ultrasonicated to create a

https://doi.org/10.30799/jnst.361.25100302

Cite this Article as: Seema Jangir, Manisha Singhal, Deepak Singh Rajawat, Band structure engineering of $BaSrTiO_3$-ZnO composites for improved water splitting performance, J. Nanosci. Tech. 10(3) (2025) 1012–1018.

homogenous slurry. A 100 µL aliquot of this slurry was drop-cast onto a pre-cleaned 1 × 1 cm^2 ITO glass substrate and spin-coated at 2500 rpm for 30 seconds. The coated substrates were dried at 100 °C for 30 minutes and subsequently annealed at 500 °C for 1 hour to enhance adhesion and crystallinity. The PEC response was assessed under light using a 500 W/m^2 LED light source. Linear sweep voltammetry (LSV) was conducted from 0 to 1.5 V at a scan rate of 50 mV/s to determine photocurrent density. Electrochemical impedance spectroscopy (EIS) was performed in the frequency range of 100 kHz to 1 Hz to evaluate the charge transfer resistance. Mott-Schottky measurements were conducted at 1 kHz over a potential range of -1 V to +1 V to understand the flat-band potential and carrier concentration. Transient photocurrent response was recorded under chopped illumination at 0.8 V vs Ag/AgCl for 300 seconds, with light on/off intervals of 10 seconds, to assess the stability and separation efficiency of charge carriers.

3. Results and Discussion

3.1 Morphological Characterization of Pure BST, ZnO and BST/ZnO Composites

The scanning electron microscope (SEM) images of pure BST shown in Fig. 4, that shows a well-developed polycrystalline surface. The grains are evenly distributed and closely packed, with little visible porosity. This suggests that the sintering process was effective, allowing the grains to grow in a controlled manner and bond tightly at their boundaries. The relatively uniform grain size also indicates that the material is stable and well-suited for use in electronic components.

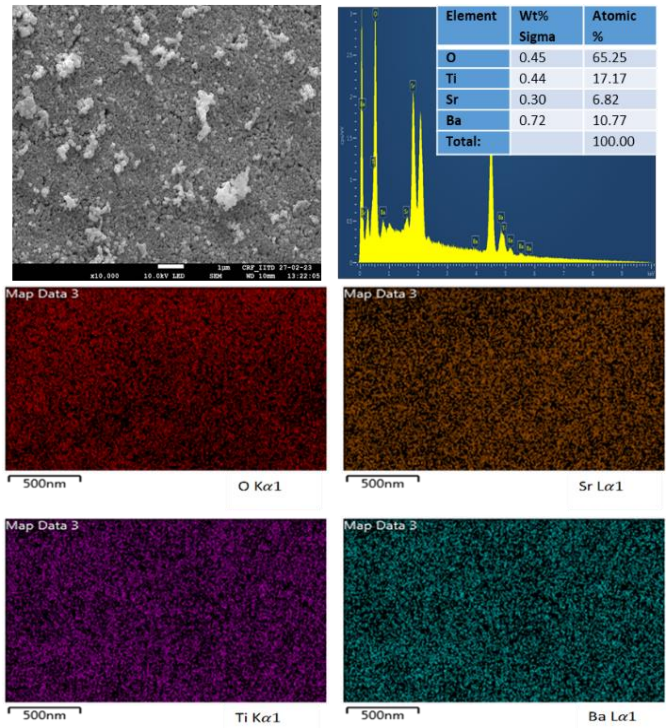

Fig. 4 SEM, EDX spectrum, quantitative analysis and elemental mapping of pure BST

The EDS spectrum reveals distinct peaks at specific energies that correspond to the characteristic X-ray emissions of the constituent elements in the sample. A strong peak at 0.525 keV confirms the presence of oxygen (O Kα), which is typical in oxide materials. Titanium (Ti) is identified by its Lα line at 0.452 keV, along with sharper peaks at 4.508 keV (Ti Kα) and 4.931 keV (Ti Kβ), indicating its presence in both low- and high-energy ranges. Strontium (Sr) is evident through its L-series peaks at 1.806 keV (Sr Lα) and 1.943 keV (Sr Lβ), while barium (Ba) contributes several distinct peaks, including 0.432 keV (Ba Mα), 4.466 keV (Ba Lα), 4.830 keV (Ba Lβ1), and 5.243 keV (Ba Lβ2). These precise peak energies align with known standards for X-ray emissions and confirm the presence of Ba, Sr, Ti, and O in the sample. The combined presence and spectral positions of these elements strongly suggest the material is a perovskite oxide.On the other hand, the SEM analysis of ZnO reveals a structure typical of the hexagonal wurtzite phase. The ZnO particles display a mix of rod-like and granular shapes and tend to stick together, forming clumps due to strong interactions between them as shown in Fig. 5. This clustering leads to a rough surface, which can affect how charges move across the material. The variation in grain shape suggests that ZnO could behave differently depending on direction, which might be useful in certain design applications.

The EDS spectrum clearly displays several characteristic peaks that confirm the presence of carbon, oxygen, zinc, and gold within the analyzed sample. A small peak at 0.277 keV corresponds to carbon, indicating either a carbon-based material or possibly a carbon coating used during sample preparation. The presence of oxygen is confirmed by a distinct peak at 0.525 keV, which is typical for oxide compounds. Zinc appears prominently with peaks at 1.012 keV, 8.638 keV, and 9.572 keV, suggesting a significant amount of zinc in the material, likely in the form of zinc oxide. Additionally, several peaks associated with gold are observed at 2.123 keV. These peaks are consistent with the known X-ray emission lines of gold and indicate that gold is also present in the sample, possibly as a coating or a structural component. The distribution and intensity of these peaks support the conclusion that the material is composed mainly of zinc and oxygen, with traces of carbon and gold, possibly forming a composite or layered structure.

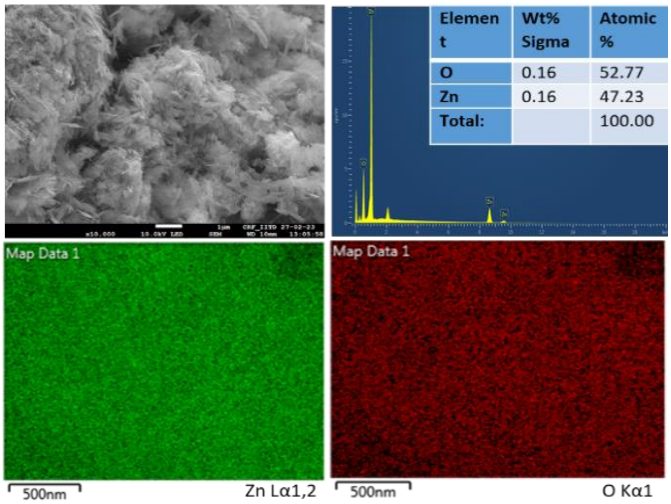

Fig. 5 SEM, EDX spectrum, quantitative analysis and elemental mapping of Pure ZnO

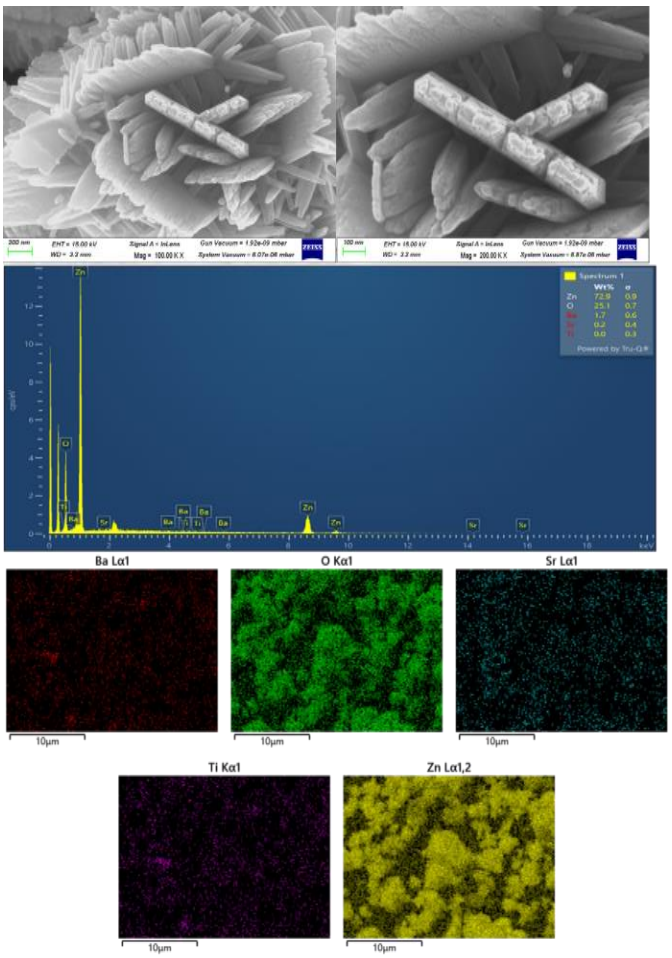

Fig. 6 SEM, EDX image, quantitative analysis and elemental mapping of BST@ZnO 3%

https://doi.org/10.30799/jnst.361.25100302

The morphological and compositional features of the BST@ZnO (3%) composite, as shown in Fig. 6, were examined using SEM-EDX analysis. The SEM images reveal well-developed rod- and plate-like structures, indicating high crystallinity and uniform surface growth. The EDX spectrum displays distinct energy peaks corresponding to the constituent elements: Ba (4.4–4.8 keV), Sr (1.8–2.0 keV and 14–15 keV), Ti (4.5–4.9 keV), Zn (8.6–9.7 keV), and O (0.5–0.6 keV). These characteristic emission peaks arise due to the release of X-ray photons when incident electrons dislodge inner-shell electrons and higher-energy electrons fall into their place. The observed peak positions confirm the presence of all expected elements in the composite, with Zn and O exhibiting dominant intensities owing to ZnO loading. Quantitative analysis further reveals that Zn accounts for the highest proportion (72.9 wt%), followed by O (25.1 wt%), with Ba, Sr, and Ti present in smaller but detectable amounts. Moreover, elemental mapping demonstrates the homogeneous distribution of all detected elements, suggesting uniform ZnO incorporation over the BST matrix. This combination of morphological and compositional evidence validates the successful synthesis of the BST@ZnO (3%) composite.

3.2 X-Ray Diffraction (XRD) Analysis

The crystalline structure and phase purity of the synthesized samples were investigated using X-ray diffraction (XRD). Fig. 7 illustrates the diffraction patterns obtained for BST, ZnO, and the BST–ZnO composites. The XRD pattern of BST (Fig. 7a) shows a series of well-defined peaks that are in good agreement with the standard JCPDS card No. 039-1395, confirming the formation of a single-phase perovskite structure [24,25]. The prominent diffraction peaks observed at 2θ values around 22.2°, 31.5°, 39.6°, 45.3°, 51.1°, 56.3°, 66.2°, and 75.0° correspond to the (100), (110), (111), (200), (210), (211), (220), and (310) planes of the cubic perovskite lattice. These reflections indicate that the BST sample is well-crystallized and free of secondary phases [26,27].

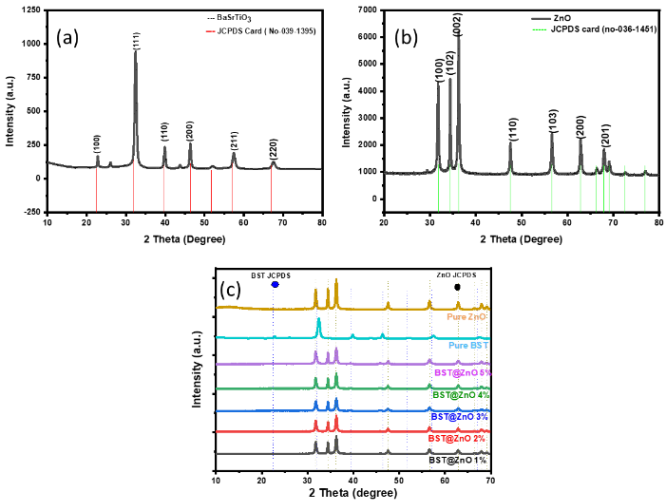

Fig. 7 XRD patterns of pure BST, pure ZnO, and BST@ZnO with varying BST (1-5%)

In comparison, the XRD pattern of ZnO in Fig. 7b matches well with the standard hexagonal wurtzite structure, as referenced by JCPDS card No. 036-1451 [28]. Characteristic peaks at 2θ values near 31.7°, 34.4°, 36.2°, 47.5°, 56.6°, 62.9°, 66.4°, 68.0°, 69.2°, 72.6°, and 77.0° can be indexed to the (100), (002), (101), (102), (110), (103), (200), (112), (201), (004), and (202) planes, respectively. The sharpness and intensity of these peaks further confirm the high crystallinity and purity of the ZnO sample [29].

The XRD pattern of the composite sample in Fig. 7(c) reveals the coexistence of diffraction peaks corresponding to both BST and ZnO phases. No additional or unidentified peaks were observed, indicating the absence of secondary phases or impurities [30]. This confirms that the composite retains the structural integrity of both constituent materials. Moreover, the absence of significant peak shifting suggests that there is no considerable lattice strain or solid solution formation between BST and ZnO, implying that the two phases coexist without significant interdiffusion. The results clearly demonstrate the successful synthesis of a biphasic composite system in which both BST and ZnO maintain their original crystal structures [31].

Analysis of the provided data, microstrain is a measure of the internal disorder and stress within a crystal lattice, while crystallite size is the physical size of the small, individual crystal grains that make up the material. Generally, there is an inverse relationship between these two properties: as crystallite size decreases, the number of grain boundaries and other defects per unit volume increases, leading to higher microstrain.

From Table 1, data for pure ZnO and pure BST supports this, as the smaller crystallites of pure BST (27.2 nm) have a significantly higher microstrain (0.2225) compared to the larger crystallites of pure ZnO (33.7 nm, 0.09651). However, this simple inverse trend is not always absolute. The BST/ZnO doped samples show a more complex behaviour; although crystallite size continues to decrease with doping, the microstrain also decreases. This suggests that the addition of ZnO is introducing a compositional effect that reduces the overall lattice strain, possibly by improving the crystal structure or filling defects, thereby dominating the effect of decreasing crystallite size. Therefore, while crystallite size is an important factor, microstrain is a result of multiple lattice imperfections, including dislocations, point defects, and chemical composition changes.

Table 1 Crystallite size, microstrain, FWHM, and dislocation density

Sample	Crystallite Size (nm)	Microstrain (ϵ)	FWHM (β)	Dislocation Density (ρ)
Pure ZnO	33.7	0.09651	0.3593	0.000880
Pure BST	27.2	0.2225	0.5986	0.001351
BST/ZNO3%	23.9	0.1025	0.3816	0.001750
BST/ZnO 5%	22.5	0.03243	0.3816	0.001975

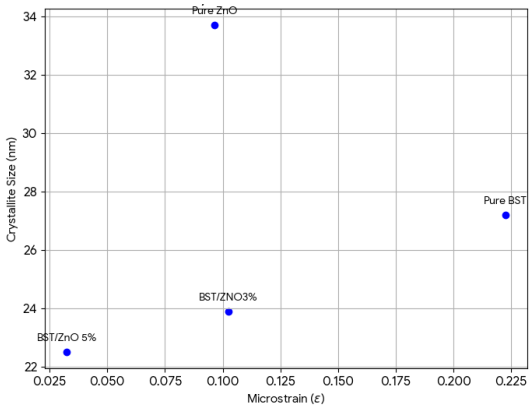

Fig. 8 Variation in crystallite size with microstrain for pure and BST/ZnO

The provided scatter plot (Fig. 8) visually represents the interplay between crystallite size and microstrain across four distinct material compositions. As observed, the pure zinc oxide (ZnO) exhibits the largest crystallite dimensions coupled with a relatively modest level of internal microstrain. Conversely, the pure barium strontium titanate (BST) demonstrates a reduction in crystallite size alongside a substantial increase in microstrain, suggesting that the finer crystalline structure in pure BST is associated with greater lattice distortions and imperfections, a trend often anticipated due to the increased density of grain boundaries and potential for defects in smaller crystallites. Intriguingly, the introduction of zinc oxide as a dopant within the BST matrix leads to a further decrease in crystallite size in both the 3% and 5% compositions. However, contrary to the initial trend observed between pure ZnO and pure BST, these doped samples exhibit a significant reduction in microstrain, with the 5% BST/ZnO sample displaying the lowest microstrain despite having the smallest crystallite size. This noteworthy deviation underscores the critical influence of compositional modifications, indicating that the incorporation of ZnO into the BST lattice likely alters the defect structure and overall stress state in a manner that mitigates internal strains, effectively overriding the typical expectation of higher strain in finer-grained materials. Therefore, while crystallite size is an important microstructural parameter influencing strain, the chemical composition and the resulting defect chemistry play a crucial and potentially dominant role in determining the overall microstrain within these materials.

3.3 UV-Visible Spectral Studies

The UV-Vis absorbance spectroscopy analysis of $BaSrTiO_3$ (BST), ZnO, and their composites was in the 300-800 nm range to evaluate their optical properties and band gap energies.

The UV-Vis spectroscopic analysis of $BaSrTiO_3$ (BST), ZnO, and their composites was conducted to evaluate their optical absorption properties and band gap energies and the results are given in Fig. 9. The study reported that pure $BaSrTiO_3$ exhibited an absorption peak around 350 nm, corresponding to a band gap of approximately 3.0 eV, while ZnO showed strong absorption near 378 nm, with a band gap of ~2.25 eV [32-34]. Upon composite formation, a slight redshift in the absorption edge was observed, indicating a reduction in band gap energy due to electronic interactions between BST and ZnO. The BST-ZnO composite exhibited a

https://doi.org/10.30799/jnst.361.25100302

Cite this Article as: Seema Jangir, Manisha Singhal, Deepak Singh Rajawat, Band structure engineering of $BaSrTiO_3$-ZnO composites for improved water splitting performance, J. Nanosci. Tech. 10(3) (2025) 1012–1018.

band gap of approximately 2.7 eV for 4% and 5% BST/ZnO composites, suggesting enhanced optical absorption and improved charge carrier dynamics. Additionally, different composite ratios of BST and ZnO demonstrated further variations in band gap values, with BST-rich composites showing band gaps around 2.7 eV and ZnO-rich composites reaching values as low as 2.9 eV. This modification in band structure enhances visible-light absorption and facilitates efficient charge carrier separation, improving the material's photocatalytic performance. The study concluded that the synergistic effects between BST and ZnO significantly enhance their optical response, making the composites promising candidates for solar-driven water splitting, photocatalysis, and environmental remediation applications.The reduction in band gap enhances visible-light absorption and charge carrier separation efficiency, improving the material's potential for photocatalytic and optoelectronic applications such as solar-driven water splitting, pollutant degradation, and energy conversion. The study concluded that BST-ZnO composites demonstrate superior optical properties compared to their individual components, making them promising materials for advanced functional applications.

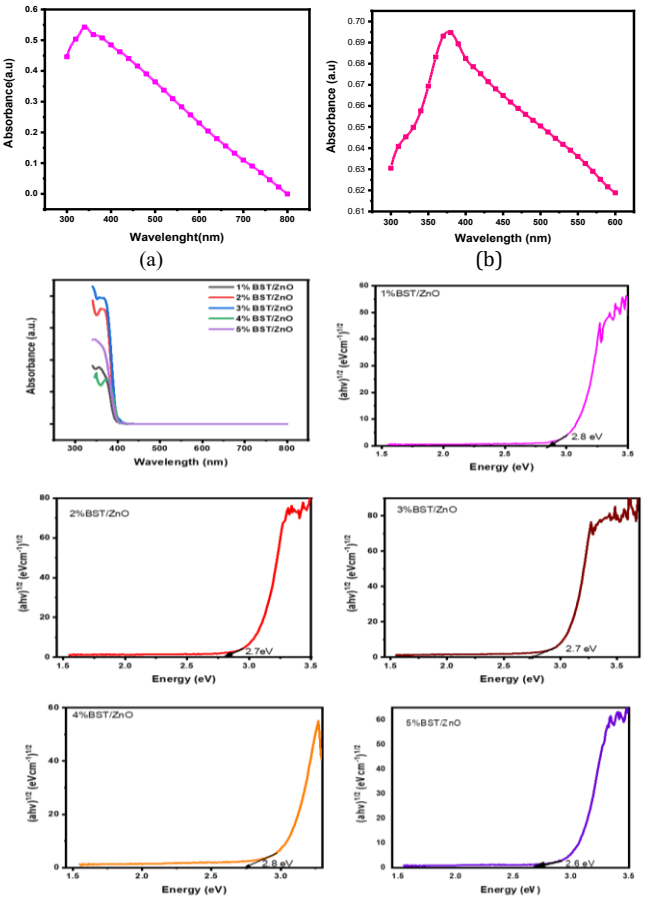

Fig. 9 UV- visible spectrum and Tauc plot of pure BST(a), ZnO(b) and BST/ZnO(c)

3.4 Photo-Electrochemical Analysis (PEC)

3.4.1 Hydrogen Evolution Reaction (HER)

PEC performance was assessed with a three-electrode setup using a Nafion-coated ITO glass electrode under a 500 W/m^2 LED light source. Linear sweep voltammetry (0-1.5 V), EIS (100 kHz to 1 Hz) and transient photocurrent measurements were conducted. Results demonstrated enhanced charge separation and photocurrent stability, confirming the composite's potential for solar-driven hydrogen production. The photoelectrochemical (PEC) performance of the $BaSrTiO_3$–ZnO composites was evaluated using three key techniques: Linear sweep voltammetry (LSV), electrochemical impedance spectroscopy (EIS), and transient photocurrent response and the results are given in Figs. 10a-c. respectively. LSV revealed that composites with higher BST content, particularly BST/ZnO 3-5%, exhibited significantly enhanced photocurrent density (2.5-2.8 mA/Cm^2) under illumination, indicating superior hydrogen evolution capabilities due to improved light absorption and charge carrier separation. The charge transport properties and electrical resistance of the photocatalyst were determined using electrochemical impedance spectroscopy (EIS). From electrochemical impedance spectroscopy (EIS), Nyquist plots were used to investigate the interfacial charge transfer resistance of pure BST, ZnO and BST/ZnO composites. In the 100 kHz–100 MHz frequency range, the charge transfer resistance is measured in the Nyquist plot between the real and imaginary parts of the resistance with an amplitude of 10 mV. In the EIS spectrum, the semicircle radius of the charge transfer resistance varies from higher to lower frequency areas. EIS measurements supported this by showing reduced charge transfer resistance in BST/ZnO 2% and 4% composites, as evidenced by smaller Nyquist semicircles, confirming efficient interfacial electron transport. The transient photocurrent density-time curves of the pure materials and composites of BST and ZnO. The illustration shows the transient photocurrents for the aforementioned samples, obtained through multiple on-off cycles lasting 10 seconds each under intermittent visible-light irradiation, with a maintained bias voltage of 0.5 V vs Ag/AgCl. Furthermore, transient photocurrent studies demonstrated the stability and efficiency of these composites, where sharp and sustained current responses under chopped light exposure indicated rapid and stable charge generation with minimal recombination. Chopped light photocurrent measurements further support this finding, showing that the 2% BST/ZnO sample exhibits the most intense and stable transient photocurrent under intermittent illumination, highlighting its superior photo-response and reduced recombination rate.

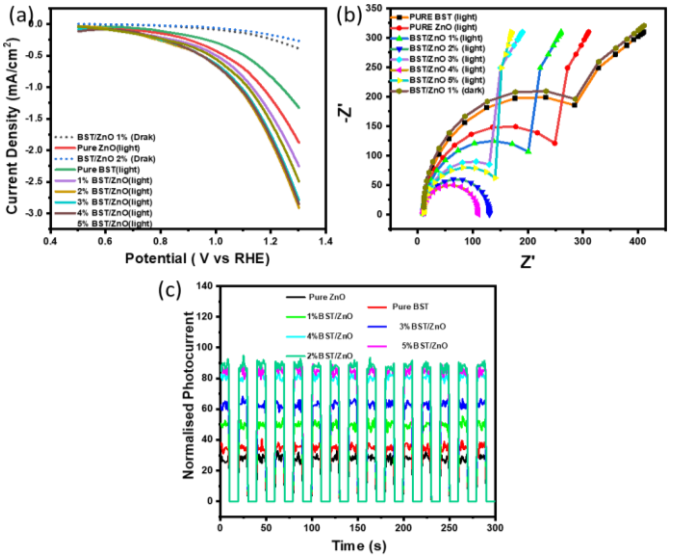

Fig.10 Linear sweep voltammetry curves (a), electrochemical impedance spectroscopy Nyquist plots at 1.23 eV Vs RHE (b) and chopped photocurrent curves (c) for HER using pure BST, ZnO and BST/ZnO composites

3.4.2 Oxygen Evolution Reaction (OER)

The results demonstrated very little OER activity for the electrodes coated with both parent materials BST and ZnO as shown in fig. 11. Linear sweep voltammetry (LSV) was performed to evaluate the photoelectrochemical (PEC) performance of BST, ZnO, and their composites by measuring photocurrent density under light. The LSV curves provide insights into the charge transport efficiency and catalytic activity of the synthesized materials. Pure BST and ZnO exhibited relatively low photocurrent densities, the low performance of these individual materials is attributed to rapid charge carrier recombination and limited light absorption. In contrast, the BST/ZnO composites demonstrated significantly enhanced photocurrent densities, confirming improved charge separation and reduced recombination. The BST/ZnO4% composite exhibited the highest photocurrent density of 0.2 mA/cm^2 at 1.23 V, nearly four times higher than both pure materials, indicating a more efficient electron-hole separation at the heterojunction interface. Similarly, BST/ZnO 5% achieved a photocurrent density of 0.15 mA/cm^2 at 1.23 V, reflecting its improved conductivity and charge mobility due to the well-integrated composite. The enhancement in photocurrent density can be attributed to the strong interfacial interactions between BST and ZnO which facilitate charge transfer and suppress recombination.

Electrochemical impedance spectroscopy (EIS) is used to understand the photo-electrochemical capabilities of different gradient compositions. More specifically, the dynamics of charge transfer that flow between the electrolyte and the surface of the materials serve as either anode or cathode. The semi-circular curvature of the Nyquist plot corresponds to the electrode/electrolyte interface and the radius of the curvature symbolizes the charge transfer resistance. Electrochemical impedance spectroscopy (EIS) was conducted to evaluate the charge transfer resistance and interfacial charge dynamics of BST, ZnO and their composites. The Nyquist plots provide insights into the charge transport

https://doi.org/10.30799/jnst.361.25100302

Cite this Article as: Seema Jangir, Manisha Singhal, Deepak Singh Rajawat, Band structure engineering of $BaSrTiO_3$-ZnO composites for improved water splitting performance, J. Nanosci. Tech. 10(3) (2025) 1012–1018.

properties, where the semicircle diameter represents the charge transfer resistance (Rct) at the electrode-electrolyte interface. A smaller semicircle corresponds to lower resistance, indicating more efficient charge transfer and improved photoelectrochemical performance. Pure BST and ZnO exhibited relatively large semicircle diameters, indicating high charge transfer resistance due to their limited conductivity and rapid charge recombination. The BST/ZnO composites (2% and 5%) demonstrated significantly reduced charge transfer resistance, confirming enhanced charge separation at the heterojunction interface. The BST/ZnO 5% exhibited the smallest semicircle indicating superior charge transport and minimal recombination losses and supporting the improved interfacial conductivity due to the well-integrated structure.

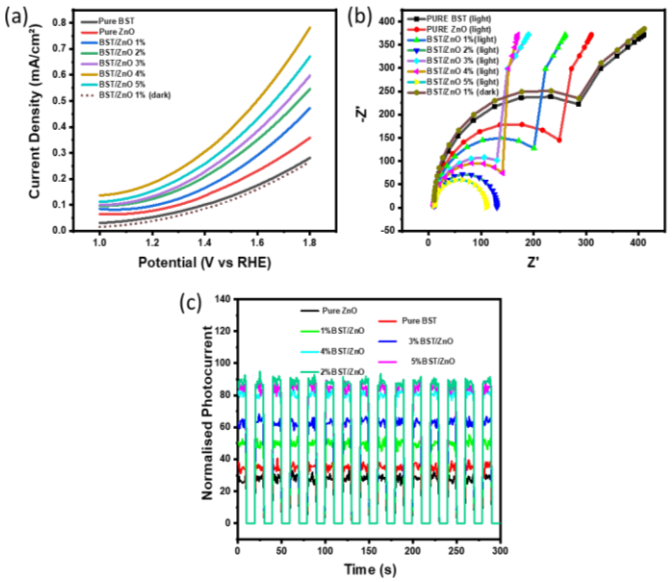

Fig. 11 Linear sweep voltammetry curves (a), electrochemical impedance spectroscopy Nyquist plots at 1.23 eV Vs RHE (b) and chopped photocurrent curves (c) for OER using Pure BST, ZnO and BST/ZnO composites

Transient current response measurements under a constant applied potential of 1.23 V demonstrate that composites sustain a stable current over time, with minimal fluctuation or degradation. These synergistic improvements position BST/ZnO composites as a highly promising and resilient catalyst for sustainable water-splitting and renewable energy application. Chopped light photocurrent measurements provide additional confirmation of this result, demonstrating that the 2% BST/ZnO composite yields the most intense and consistent transient photocurrent response when subjected to intermittent illumination. This enhanced and stable photo-response strongly suggests more efficient charge separation and a significant reduction in electron–hole recombination.

4. Conclusion

In this present work, BST-ZnO composite nanomaterials were synthesized successfully using a combination of sol-gel and co-precipitation methods to improve photocatalytic water splitting for hydrogen production. The composites, which showed distinct but integrated crystalline phases, exhibited a reduced band gap (2.7-2.9 eV) and enhanced visible light absorption compared to the individual components. This band gap tuning, along with the favourable nanostructured morphology and high chemical purity, contributed to a significant increase in photocatalytic performance. Photoelectrochemical analysis confirmed that the composites, especially those with 3-5% BST content, demonstrated a higher photocurrent density and lower charge transfer resistance, indicating improved charge separation and transport at the interface. The study concludes that engineering these hybrid materials via compositional and morphological control is an effective strategy for creating high-performance photocatalysts for sustainable hydrogen production, paving the way for further research into co-catalyst integration and advanced fabrication techniques.

References

[1] S. Kribalis, P.E. Tsakiridis, C. Dedeloudis, E. Hristoforou, Structural and electrical characterization of barium strontium titanate films prepared by sol-gel technique on brass (CuZn) substrate, J. Optoelectron. Adv. Mater. 8 (2006) 1475-1478.
[2] R. Joy, S. Haridas, Strontium titanate aided water splitting: An overview of current scenario, Int. J. Hydrog. Ener. 46 (2020) 1879-1903.
[3] M. Faraji, M. Yousefi, S. Yousefzadeh, M. Zirak, N. Naseri, T.H. Jeon, W. Choi, A.Z. Moshfegh, Two-dimensional materials in semiconductor photoelectrocatalytic systems for water splitting, Ener. Environ. Sci. 12 (2019) 59-95.
[4] M. Singhal, S. Jangir, A. Charan, R. Sharma, S. Upadhyay, D.S. Rajawat, Photoelectrochemical performance of $BiV_{1-x}Cr_xO_4$ in water splitting: Experimental and first principles study. J. Ind. Chem. Soc. 102 (2025) 102187.
[5] D. Hertkorn, C. Megnin, C. Müller, T. Hanemann, H. Reinecke, Light intensity influence on strontium titanate-based photo-electrochemical cells, Ceram. Silikáty 61 (2017) 179-182.
[6] K. Nakashima, M. Kera, I. Fujii, S. Wada, A new approach for the preparation of $SrTiO_3$ nanocubes, Ceram. Int. 39 (2012) 3231-3234.
[7] J. Joy, J.S. Mathew, S.C. George, Nanomaterials for photoelectrochemical water splitting - review, Int. J. Hydrog. Ener. 43 (2018) 4804-4817.
[8] P. Jayabal, V. Sasirekha, J. Mayandi, K. Jeganathan, A facile hydrothermal synthesis of $SrTiO_3$ for dye sensitized solar cell application, J. Alloy. Compd. 586 (2014) 456-461.
[9] G. Wu, P. Li, D. Xu, B. Luo, Hydrothermal synthesis and visible-light-driven photocatalytic degradation for tetracycline of Mn-doped $SrTiO_3$ nanocubes, Appl. Surf. Sci. 333 (2015) 39-47.
[10] F. Cai, Y. Tang, F. Chen, Y. Yan, W. Shi, Enhanced visible-light-driven photocatalytic degradation of tetracycline by Cr^{3+}-doped $SrTiO_3$ cubic nanoparticles, RSC Adv. 5 (2015) 21290-21296.
[11] J. Zhu, Y. Zhang, L. Shen, J. Li, L. Li, Hydrothermal synthesis of Nb^{5+}-doped $SrTiO_3$ mesoporous nanospheres with greater photocatalytic efficiency for Cr(VI) reduction, Powder Technol. 410 (2022) 117886.
[12] J. Roque-Ruiz, Sol-gel synthesis of strontium titanate nanofibers by electrospinning, J. Ceram. Sci. Technol. 10 (2019) 29-38.
[13] S. Gholamrezaei, M.S. Niasari, M. Dadkhah, New modified sol–gel method for preparation $SrTiO_3$ nanostructures and their application in dye-sensitized solar cells, J. Mater. Sci. Mater. Electron. 27 (2015) 118-125.
[14] L. Zhu, W. Gu, J. Chen, H. Liu, Y. Zhang, Q. Wu, Improving the photocatalytic hydrogen production of $SrTiO_3$ by in situ loading ethylene glycol as a co-catalyst, Inorg. Chem. Front. 7 (2020) 4133-4141.
[15] A. Jia, X. Liang, Z. Su, Synthesis and the effect of calcination temperature on the physical-chemical properties and photocatalytic activities of Ni, La codoped $SrTiO_3$, J. Hazard. Mater. 178 (2010) 233-242.
[16] Q. Hu, J. Niu, K. Zhang, M. Yao, Fabrication of Mn-doped $SrTiO_3$/carbon fiber with oxygen vacancy for enhanced photocatalytic hydrogen evolution, Mater. 15 (2022) 4723-4738.
[17] Z. Ying, S. Chen, T. Peng, Fabrication of an Fe-doped $SrTiO_3$ photocatalyst with enhanced dinitrogen photofixation performance, Eur. J. Inorg. Chem. 2019 (2019) 2182-2192.
[18] F. Rechberger, G. Ilari, C. Willa, Processing of Cr doped $SrTiO_3$ nanoparticles into high surface area aerogels and thin films, Mater. Chem. Front. 1 (2017) 1662-1667.
[19] M. Junaid, K.M. Batoo, S.G. Hussain, S. Hussain, Structure, morphology, dielectric study of Ba-doped $SrTiO_3$ by sol-gel method for optical applications, Results Chem. 6 (2023) 101177.
[20] A. Mishra, H. Parangusan, J. Bhadra, Z. Ahmed, Synthesis and photoelectrochemical performance of Co doped $SrTiO_3$ nanostructures photoanode, Environ. Prog. Sustain. Ener. 42 (2023) e14186.
[21] G.L. He, Y.H. Zhong, Y.H. Xu, One-pot hydrothermal synthesis of $SrTiO_3$-reduced graphene oxide composites with enhanced photocatalytic activity for hydrogen production, J. Mol. Catal. A: Chem. 423 (2016) 70-76.
[22] Y. He, S. Ouyang, Z. Li, Sol–gel hydrothermal synthesis of visible-light-driven Cr-doped $SrTiO_3$ for efficient hydrogen production, J. Mater. Chem. 21 (2011) 11347-11351.
[23] T. Surendar, S. Kumar, O. Anjaneyulu, V. Shanker, Synthesis of Cr and La-codoped $SrTiO_3$ nanoparticles for enhanced photocatalytic performance under sunlight irradiation, Phys. Chem. Chem. Phys. 16 (2014) 23819-23828.
[24] W. Tuff, P. Manghera, J. Tilghman, E. Van Fossen, S. Chowdhury, S. Ahmed, S. Banerjee, $BaTiO_3$–Epoxy–ZnO-based multifunctional composites: Variation in electron transport properties due to the interaction of ZnO nanoparticles with the composite microstructure, J. Electron. Mater. 48 (2019) 6584-6595.
[25] M. Ghasemifard, M.E. Abrishami, M. Iziy, Effect of different dopants Ba and Ag on the properties of $SrTiO_3$ nanopowders, Results Phys. 5 (2015) 309-313.
[26] A. Sadeghzadeh Attar, E. Salehi Sichani, S. Sharafi, Structural and dielectric properties of Bi-doped barium strontium titanate nanopowders synthesized by sol-gel method, J. Mater. Res. Technol. 216 (2016) 1-8.
[27] S. Boumaza, A. Boudjemaa, A. Bouguelia, R. Bouarab, M. Trari, Visible light induced hydrogen evolution on new hetero-system $ZnFe_2O_4$/$SrTiO_3$, Appl. Ener. 87 (2010) 2230-2236.
[28] A.D. Hussein, R.S. Sabry, PVDF: ZnO/$BaTiO_3$ as high out-put piezoelectric nanogenerator, Polym. Test. 79(17) (2019) 106001.
[29] K. Guo, Z. Liu, Y. Wang, Y. Zhao, Y. Xiao, et al., Fabrication of ZnO/$SrTiO_3$ nanoarrays and its photoelectrochemical performances, Int. J. Hydrog. Ener. 39 (2014) 13408-13414.
[30] B. Ben Salem, G. Essalah, S. Ben Ameur, B. Duponchel, H. Guermazi, S. Guermazi, G. Leroy, Synthesis and comparative study of the structural and optical properties of binary ZnO-based composites for environmental applications, RSC Adv. 13 (2023) 6287-6303.
[31] J. Li, Y. Wang, Z. Xu, Z. Chen, Ferroelectric and piezoelectric enhancement in ZnO/$Ba_{0.5}Sr_{0.5}TiO_3$ heterostructure thin films, J. Alloys Compd. 904 (2022) 164027.
[32] K. Kandpal, N. Gupta, J. Singh, C. Shekhar, Study of ZnO/BST interface for thin-film transistor (TFT) applications, Surf. Interf. 23 (2021) 100996.

https://doi.org/10.30799/jnst.361.25100302

Cite this Article as: Seema Jangir, Manisha Singhal, Deepak Singh Rajawat, Band structure engineering of $BaSrTiO_3$-ZnO composites for improved water splitting performance, J. Nanosci. Tech. 10(3) (2025) 1012–1018.

[33] J. Guo, X. Wang, Z. Jia, J. Wang, C. Chen, Nonlinear electrical properties and field dependency of BST and nano-ZnO-doped silicone rubber composites, Molecules 23 (2018) 3153.
[34] K.T. Kang, I.D. Kim, M.H. Lim, H.G. Kim, J.M. Hong, Annealing effect on dielectric and leakage current characteristics of Mn-doped $Ba_{0.6}Sr_{0.4}TiO_3$ thin films as gate insulators for low voltage ZnO thin film transistor, Thin Sol. Film. 516 (2008) 1218-1222.
[35] G. Liu, W. Jiang, J. Jiao, L. Liu, Z. Wang, J. Cai, W. Luo, C. Song, The investigation of electrical properties and microstructure of ZnO-doped $Ba_{0.9}Sr_{0.1}TiO_3$ ceramics, J. Adv. Dielectr. 7 (2017) 1750007.
[36] A. Malasi, N. Nanda, S. Swain, P. Kumar, Tailoring breakdown behaviour in BST-xMgO ceramics for energy storage applications, J. Alloys Compd. 1038 (2025) 182737.
[37] K. Kandpal, N. Gupta, J. Singh, C. Shekhar, Study of ZnO/BST interface for thin-film transistor (TFT) applications, Surf. Interf. 23 (2021) 100996.
[38] K. Guo, Z. Liu, Y. Wang, Y. Zhao, Y. Xiao, J. Han, Y. Li, B. Wang, T. Cui, Fabrication of $ZnO/SrTiO_3$ nanoarrays and its photoelectrochemical performances, Int. J. Hydrog. Ener. 39 (2014) 13447-13453.
[39] R. Bashiri, N.M. Mohamed, N.A. Suhaimi, M.U. Shahid, C.F. Kait, S. Sufian, M. Khatani, A. Mumtaz, Photoelectrochemical water splitting with tailored TiO_2 /$SrTiO_3$@g–C_3N_4 heterostructure nanorod in photoelectrochemical cell, Diam. Relat. Mater. 85 (2018) 5-12.

https://doi.org/10.30799/jnst.361.25100302

Cite this Article as: Seema Jangir, Manisha Singhal, Deepak Singh Rajawat, Band structure engineering of $BaSrTiO_3$-ZnO composites for improved water splitting performance, J. Nanosci. Tech. 10(3) (2025) 1012–1018.